Article

Anodic Potential and Conversion Chemistry of Anhydrous Iron (II) Oxalate in Na-Ion Batteries

Vasilii Gromov [1], Atlas Noubir [1], Fatemeh Keshavarz [1,*], Ekaterina Laakso [2], Bernardo Barbiellini [1,3] and Arun Bansil [3]

[1] Department of Physics, School of Engineering Science, LUT University, FI-53851 Lappeenranta, Finland; gromovv.vasilii@gmail.com (V.G.); atlasn789@gmail.com (A.N.); bernardo.barbiellini@lut.fi (B.B.)
[2] Separation Science, School of Engineering Science, LUT University, FI-53851 Lappeenranta, Finland; ekaterina.laakso@lut.fi
[3] Department of Physics, Northeastern University, Boston, MA 02115, USA; ar.bansil@northeastern.edu
[*] Correspondence: fatemeh.keshavarz@lut.fi

Abstract: Anhydrous ferrous (II) oxalate (AFO) outperforms its hydrated form when used as an anode material in Li-ion batteries (LIBs). With the increasing interest in Na-ion batteries (NIBs) in mind, we examine the potential of AFO as the anode in NIBs through first principles calculations involving both periodic and non-periodic structures. Our analysis based on periodic (non-periodic) modeling scheme shows that the AFO anode generates a low reaction potential of 1.22 V (1.45 V) in the NIBs, and 1.34 V (1.24 V) in the LIBs, which is much lower than the potential of NIBs with mixed oxalates. The conversion mechanism in the underlying electrochemical process involves the reduction of Fe^{2+} with the addition of Na or Li. Such conversion electrodes can achieve high capacities through the Fe^{2+} valence states of iron.

Keywords: Na-ion battery; humboldtine; iron oxalate; anode; electrochemical potential; conversion mechanism; first-principles calculations; density functional theory (DFT)

1. Introduction

The increasing interest in electrical vehicles is motivating the further development of batteries, especially the Li-ion (LIB) batteries, with rational energy distribution and efficient charging and discharging properties [1]. LIBs offer several important advantages, including high energy and power densities, long life cycles, high stability, high voltage discharge and low self-discharge rates [2–4]. However, their electrochemical response is sensitive to material fatigue and temperature [5]. Since lithium is not an abundant resource, Na-ion batteries (NIBs) are replacing LIBs. This trend is justified by the availability of sodium in large quantities and its lower cost [6,7]. Cost and abundance are, of course, important factors for the grid-scale production of energy storage systems [8]. For these reasons, LIBs and NIBs could soon compete to dominate the energy industry [9]. However, LIBs and NIBs present their own relative advantages and disadvantages, so the search for cost effective and efficient anode, cathode and electrolyte materials can be expected to continue.

Recently, metal oxalates have appeared on the scene as a green alternative to anode material in metal-ion batteries, providing excellent cycling stability and high energy density [10]. Transition metal oxides can be considered as sustainable energy storage materials because their oxalate anions ($C_2O_4^{2-}$) can be produced from carbon dioxide and act as a CO_2 reservoir, reducing the overall CO_2 content of the atmosphere. They can also serve as a green precursor for the production of metal-oxide particles through thermal degradation [11]. Some metal oxalates, such as the copper and iron oxalates [11–13], present outstanding properties for battery applications by storing Li and Na ions and generating electrochemical energy through a *conversion mechanism* rather than an intercalation [14–16].

During reversible intercalation, metal ions, such as Li or Na, interact with the electrode material and exchange electrons with the redox orbitals of the transition metal atoms without inducing major structural changes. Therefore, the number of exchanged electrons and the associated redox activity of the material is controlled by the crystal structure of the material, which does not undergo irreversible degradation [15]. In contrast, in the conversion mechanism, when the Li/Na ions interact with the anode material, the oxidized metal centers reduce to their metallic state and the anode turns into metal atoms embedded in a network of Li/Na oxalate. For sodium, the conversion reaction can be written as

$$\mathrm{MC_xO_y} + 2\mathrm{Na}^+ + 2\mathrm{e}^+ \rightarrow \mathrm{Na_2C_xO_y} + \mathrm{M}, \tag{1}$$

where M represents the metal. Although the conversion reaction would appear to be irreversible at room temperature, it turns is reversible in some materials, such as the metal oxalates [15]. The reason for this is that the full reduction of the transition metal atoms in the material leads to the formation of metal nanoparticles with a high interfacial surface area and strong activity to decompose the surrounding Na/Li oxalate phase [15,17]. The conversion process can thus provide a higher capacity compared to the intercalation processes. However, this results in the formation of some intermediate compounds, which yield deviations from the theoretical electrochemical potential values. It also involves the formation of nanoparticles and a significant increase in the surface area, so that a voltage hysteresis can be expected [15].

　　Metal oxalates can support similar conversion mechanisms. As an example, we consider the ferrous oxalate dihydrate (FOD) or the iron (II) oxalate dihydrate ($\mathrm{FeC_2O_4 \cdot 2H_2O}$) (humboldtine). This material is promising for clean energy applications, and can also be mined or easily synthesized [18]. Its high photocatalytic activity [19,20] and proton conductivity [21] justifies its use in photocatalysis and wastewater treatment [22,23]. Moreover, due to its relatively low thermal stability [24], it is used as a precursor to synthesize various Fe-containing battery materials [25,26]. FOD has also shown promising properties for Li storage and LIB anode applications [27–29]. An outstanding feature of FOD is that its hydration level has a direct impact on its anodic activity in LIBs. In an earlier computational study [29], we showed that anhydrous ferrous oxalate (AFO) ($\mathrm{FeC_2O_4}$) supports a higher Li storage capacity and a lower voltage compared to its fully hydrated state (FOD), and even its partially hydrated counterpart, in accordance with experimental studies [13,27]. The negative impact of structural water on FOD's electrochemical activity is a direct outcome of Li hydration by the water molecules and their inhibitory role in Li interaction with the iron oxalate chains [29]. It is also related to the interaction of structural water with $\mathrm{LiPF_6}$ and HF production [13]. Therefore, AFO offers higher stability and more favorable electrochemical potential relative to FOD [13,29].

　　As previously noted, NIBs can offer advantages over the LIBs. With this motivation, we evaluate the performance of AFO (rather than FOD) as an anode material in NIBs and compare its electrochemical properties to those of the corresponding LIBs. We also **discuss** the underlying electrochemical mechanism to evaluate the potential impact of conversion chemistry on the performance of ferrous oxalates. Our study provides an insight into the favorable reaction potential of AFO in Na-ion batteries.

2. Computational Method

　　The activity of AFO for potential application in Na-ion batteries was studied using both periodic and non-periodic quantum mechanical calculations. Periodic and non-periodic approaches can highlight different aspects of the electronic structure and thermodynamics of materials [30]. The inclusion of periodicity can improve property predictions [31,32]. Therefore, to gain a more robust understanding of the effects of Na insertion in AFO chains and the underlying electrochemical mechanism, we considered both approaches in the absence of experimental data on AFO-based NIBs. Our combinatorial approach also allowed us to isolate the effect of metal-oxalate periodicity on the Na interaction with AFO chains. To compare the activity of AFO as an anode of NIBs vs. LIBs, we also performed

complementary calculations involving Li interactions with AFO. We divide the discussion of these details into the following subsections.

2.1. Non-Periodic Calculations

Non-periodic calculations were performed on a truncated model of AFO using Gaussian 16 A.03 [33]. The cluster model (Figure 1) and the optimal computational level (i.e., PBE/cc-pVDZ [34] + D3 Grimme's dispersion correction [35]) were retrieved from and validated in our earlier study on humboldtine and its partially and fully dehydrated counterparts [29]. First, the electronic structure and geometry of the Na^0-free AFO model were relaxed. Then, a system containing a Na^0 atom near the central Fe^{2+} ion of AFO was optimized. Notably, our previous study of the Li/humboldtine system [29] showed that configurational changes in the starting Na/AFO system by relocating the metal ion/atom with respect to the central Fe atom does not change the final optimized structure. Therefore, we did not explore configurational changes in the present cluster-based calculations. For both systems, several potential spin states were considered. The spin state with no imaginary frequency, insignificant spin contamination, and the lowest electronic and Gibbs free energy was identified as the ground state. The spin-state results are presented in Table S1 of the Supporting Information. To better understand the nature of the conversion mechanism, we also studied a system with two Na^0 atoms near the central Fe. We did not consider the intercalation of Na^+ because our previous work on Li^0 and Li^+ intercalations into hydrated and dehydrated humboldtine showed that the application of both Li oxidation states provides similar electrochemical potential changes [29]. We also did not include the effect of basis set superposition error (BSSE) on the final adsorption energies and voltage values. The reason for this is that our earlier study of Li interactions with humboldtine [29] showed that our non-periodic model (without BSSE inclusion) provides an accurate prediction of the electrochemical potential. The Bernardi and Boys approach, which is the counterpoise method used by Gaussian to calculate BSSE, is sensitive to the division of the system into different fragments and its results exhibit variations [36]. Moreover, our estimation of the effect of the BSSE on the final voltage found only a -0.12 V difference for the AFO system with one Na and -0.17 V difference for two Na atoms, and thus did not affect our conclusions significantly.

2.2. Periodic Calculations

To evaluate the effect of crystal periodicity on the electrochemical results and undertake a comprehensive analysis, we simulated periodic Na^0-free and Na^0-containing AFO systems with the Quantum Espresso software [37]. As the crystal structure of AFO is not available, we started with the unit cell structure of α-monoclinic humboldtine [38]. Then, we removed the water molecules, relaxed the atoms and obtained the equilibrium monoclinic AFO unit cell shown in Figure 1. For the relaxation process, we considered a variable (non-fixed) cell, and minimized its stress. The Broyden–Fletcher–Goldfarb–Shanno (BFGS) algorithm [39] was used in this optimization. The ion-convergence criterion was 10^{-3} Ry Bohr^{-1}. The Quantum Espresso calculations used the PBE functional (as in our non-periodic calculations) and a grid of $1 \times 2 \times 2$ k-points over the Brillouin zone. The fully relativistic rrkjus pseudo-potentials (available in the Quantum Espresso's library) were used and a cut-off energy of 80 eV was applied. To ensure the correct positioning of the Na^0 atom in the AFO structure, we tried several starting configurations, but the results converged to a highly similar structure in all cases.
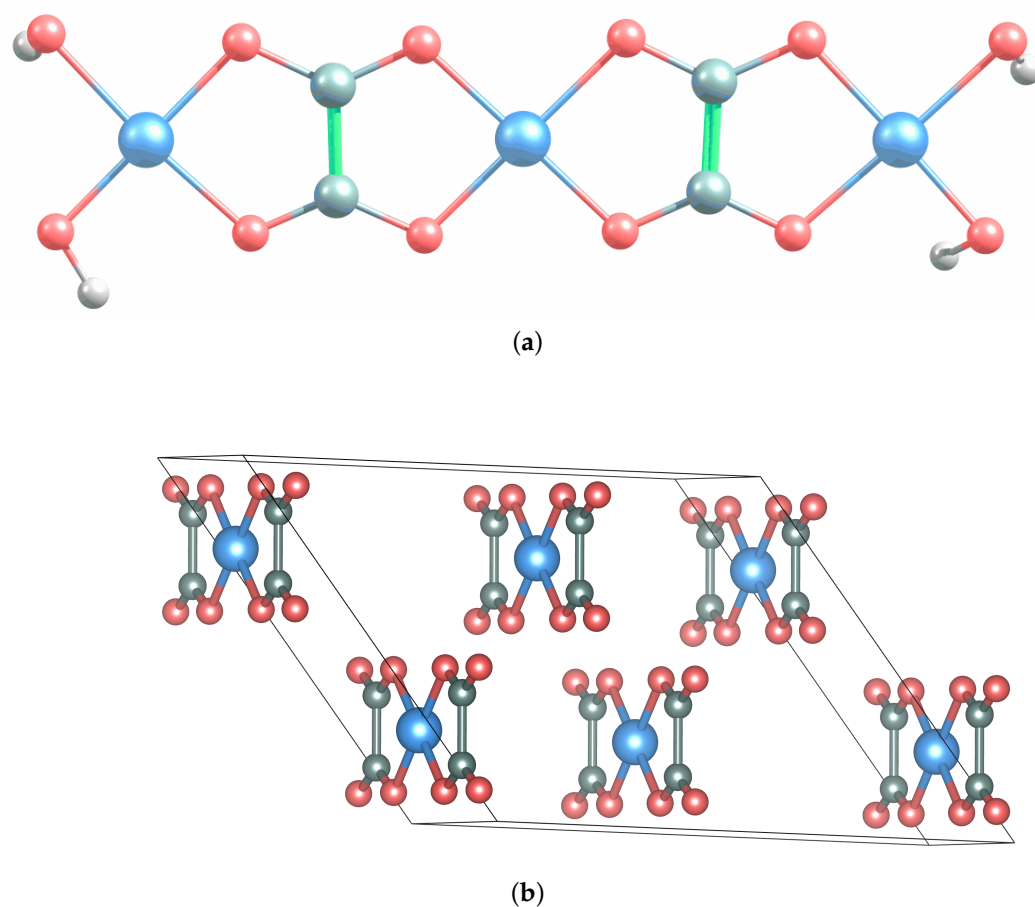
(a)

(b)

Figure 1. Structure of AFO. (**a**): truncated model. (**b**): periodic unit cell after structural optimization. (Color code: Fe: blue, C: grey, O: red, and H: light grey/white). The Bravais lattice vectors are $\mathbf{b}_1 = (12.011; 0; 0)$, $\mathbf{b}_2 = (0; 5.557; 0)$ and $\mathbf{b}_3 = (-6.179; 0; 7.760)$. The units are Å.

3. Results and Discussion

3.1. Na Interaction with AFO

To understand electronic structure changes in an AFO-based NIB, we first focus on the Na–atom interaction with the AFO structure. The Na equilibrium positions obtained from the periodic and non-periodic calculations are shown in Figure 2. These results reveal that Na interacts with AFO by bridging two oxalate anions attached to the same iron cation. The trend is similar to the behavior of Li^0 and Li^+ [29]. Both Li and Na prefer locations between the oxygen atoms of two neighboring oxalate groups. When the AFO chains are extended to a multi-chain crystal structure, the cluster-based model becomes a 3D periodic system, where Na does not bridge the oxalates of only one AFO chain. In fact, the Na atom's equilibrium position is located between the adjacent oxalate groups of the two parallel chains. This insertion of Na leads to a significant change in the lattice structure of AFO and changes the monoclinic unit cell of AFO to an asymmetric lattice (Figures 1 and 2).
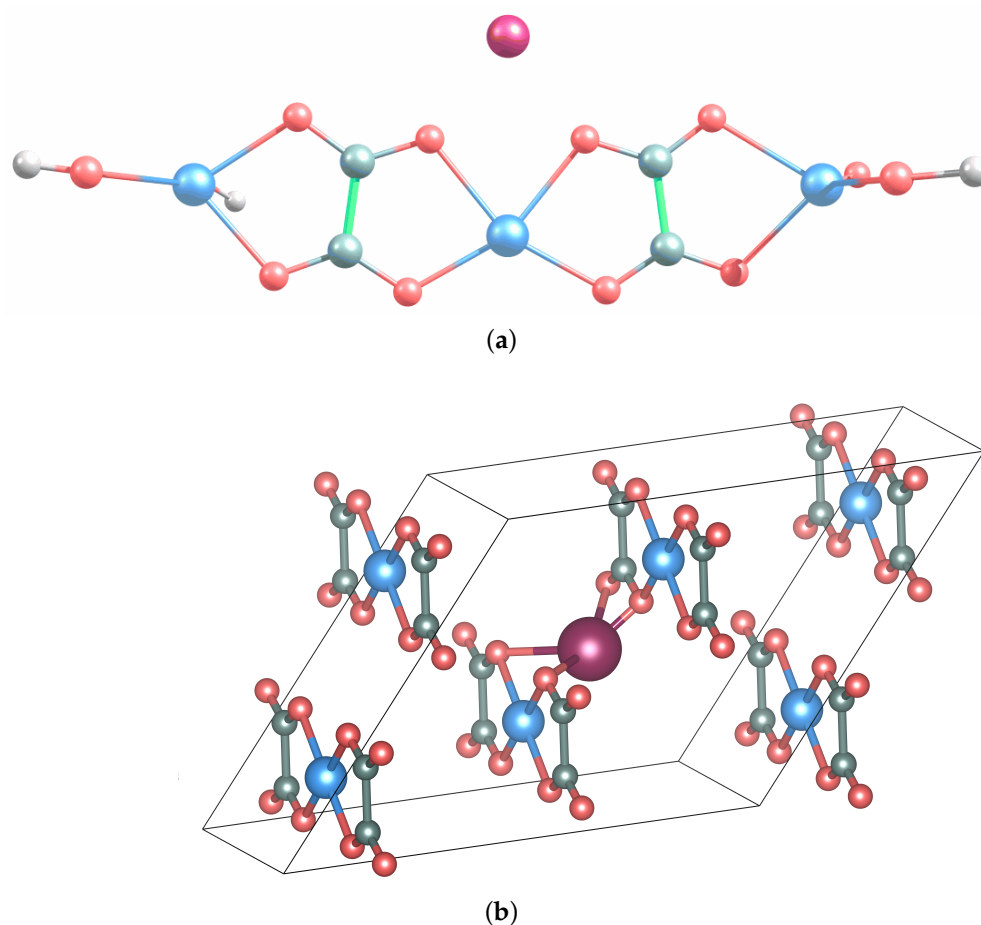
(a)

(b)

Figure 2. Structure of AFO with inserted Na. (**a**): truncated model. (**b**): periodic unit cell. (Color code: Fe: blue, C: grey, O: red, and H: light grey/white). The Bravais lattice vectors are $\mathbf{b}_1 = (12.992; 1.555; -2.304)$, $\mathbf{b}_2 = (0.507; 4.832; 0)$ and $\mathbf{b}_3 = (-7.706; 0.875, 7.610)$. The units are Å.

3.2. Conversion Mechanism

The insertion of Li and Na produces changes in the electronic structure of AFO. The density of states (DOS) of periodic AFO after Li and Na insertion displays an increased metallic character (Figure 3). The calculated band structure of pristine AFO reveals an energy gap of 1.06 eV at the Γ point. This gap reduces to 0.87 eV upon Na^0 insertion and to 0.32 eV upon Li^0 insertion. In the case of the non-periodic AFO chain, the energy gap is estimated as the energy difference between the highest occupied molecular orbital (HOMO) and the lowest unoccupied molecular orbital (LUMO). The HOMO-LUMO gap in pristine AFO is 2.21 eV, and it reduces to 1.17 eV upon Li^0 insertion and to 2.06 eV upon Na^0 insertion. The energy-gap differences between the periodic and non-periodic results can be attributed to gap-scaling effects in nano-systems [40]. However, despite these differences, both computational schemes agree in the identification of significant changes in the electronic structure of AFO resulting from the Li/Na insertion. The band gap reductions and the overall modifications of the DOS indicate a clear increase in the metallic character upon Na/Li doping.
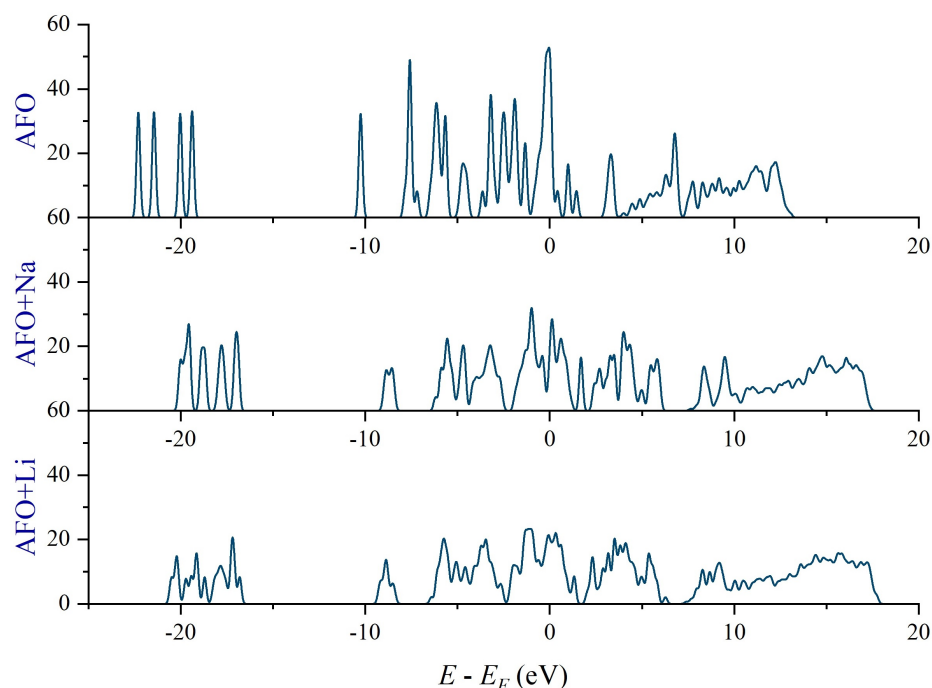
Figure 3. DOS profiles of pristine AFO and Na/Li doped AFO. The DOS profile of pristine AFO is already slightly metallic within the PBE approximation, and it becomes more metallic with both Li and Na addition.

To gain insight into the conversion mechanism, we considered the truncated model and added a second Na to the system. When a second metal ion was added, we optimized the structure at different spin states; see Table S1. For the 9tet system, which refers to 8 unpaired electrons and 2 Na^0 atoms, we observed a planar chain. However, starting from the 11tet spin state (10 unpaired electrons), the chain started to deviate from the planar geometry. In the 13tet state (12 unpaired electrons), the chain formed a ring around the axial Na^0 atoms. This state is the ground energy-state but the strong distortion of the chain is probably a spurious effect produced by finite size errors. The observed structural change might be attributed to the gradual formation of the $Li_2Fe(C_2O_4)_2$ intermediate compound, as well as the creation of an amorphous state with low degree of crystallinity, as indicated by the FTIR results of Zhang et al. [13].

With the addition of the first and second Na^0 atoms, the HOMO-LUMO gap of the ground-state structure reduces from 2.21 eV to 2.06 eV and 1.88 eV, respectively. This decreasing trend is consistent with the promotion of metallic properties in the conversion chemistry. In terms of atomic charge estimated using the Atomic Polarization Tensor (APT) scheme, the addition of one Na^0 atom to the system reduces the charge of the central Fe atom from 1.31 to 0.54 C. However, the drastic changes in the structure of AFO upon the addition of the second Na^0 increase the charge of the central Fe to 0.78 C. The general decrease in atomic charge, particularly for the system with 1 Na^0, indicates Fe reduction as a result of conversion. This also shows up in the trend of the total charge of the three Fe atoms in the Na^0-free system (4.08 C) and the system with one (2.58 C) and two (2.75 C) Na^0 atoms. To remove these spurious structural effects, one can constrain the truncated model to a planar or quasi-planar geometry in the 9tet and 11tet states, respectively. The HOMO-LUMO gap of the AFO system with 2 Na^0 atoms is 0.21 eV at the 9tet state, with the central Fe's atomic charge being 0.06 C. The HOMO-LUMO gap and central Fe's charge in the 11tet AFO + 2Na^0 system are 1.68 eV and 0.64 C, respectively. These results provide clear trends for the transition to the metallic state.

3.3. Electrochemical Potential

To predict the open-circuit voltage (OCV) generated upon the addition of Na and Li to AFO, we first calculated the adsorption energies (ΔE) using the energies of the Na/Li-AFO system with $x = 1$ Na or Li ions (M) ($E_{AFO/xM}$), AFO (E_{AFO}) and the Na/Li ion (E_M):

$$\Delta E = E_{AFO/xM} - E_{AFO} - xE_M \qquad (2)$$

Considering the periodic system, the adsorption energies for Na and Li were calculated as -2.35 eV and -2.99 eV, respectively, indicating a stronger adsorption for Li. Our calculations on the non-periodic AFO model resulted in adsorption energies of -2.58 eV and -2.89 eV [29] for single Na and Li atoms, respectively. Both computational methods provided similar results and indicated stronger Li adsorption. Next, we calculated the OCV (ΔV) values for both the AFO-based Na and Li-ion batteries [41,42] using the formula

$$\Delta V = -(E_{AFO/xM} - E_{AFO} - xE_{M\text{-}bulk})/xne, \qquad (3)$$

where $E_{M\text{-}bulk}$ is the energy of bulk Na or Li metal, n is the highest oxidation state of the cation (=1), and e is the electron charge. The energy $E_{M\text{-}bulk}$ was obtained from the cohesion energy (E_{coh}) of Na (1.13 eV) and Li (1.65 eV) metals [43], and the energy of the Na/Li (M) atom (E_M) [44,45] using the relationship:

$$\Delta E_{coh} = E_M - E_{M\text{-}bulk}. \qquad (4)$$

The OCV values for the periodic (non-periodic) AFO anode were found to be 1.22 ± 0.01 V (1.45 V) for the NIB and 1.34 ± 0.01 V (1.24 V [29]) for the LIB. The lower the voltage generated by an anode, the better the battery performance [46]. The periodic calculations yield a lower voltage generated by the AFO anode in NIBs, while the non-periodic calculations indicate a lower voltage for the LIBs. To the best of our knowledge, there are no experimental data on the potential of AFO anodes in NIBs. However, Ang et al. [47] report that the cocoon and rod-shaped AFO anodes lead to two anodic reaction peaks at 0.76 and 1.21 V, respectively, and 0.73 and 1.23 V in LIBs, over the potential range of 0–3 V (vs. $Li^+ | Li$). These point to the non-periodic calculations as a more reliable computational approach, the appeal of the periodic computations notwithstanding. In either case, our calculations agree well with the experimentally observed second peak noted above, but indicate just one potential peak and minor potential differences. These discrepancies partly result from the neglect in our calculations of the micro-environmental effects arising from electrolyte, temperature, and ion concentration, and also the fact that we ignored Li^+ in our calculations. In fact, the experimentally observed peak appearing at around 0.73–0.76 V is consistent with the OCV observed for the addition of Li^+ to AFO in our earlier non-periodic calculations, yielding a comparable corresponding value of value of 0.70 V [29]. Our findings thus agree with those of Ang et al. in that the two aforementioned peaks arise from different oxidation steps in the anodic process [47]. Because of the conflict between the preference of AFO for NIBs over LIBs and the absence of one of the oxidation steps from our calculations, we are not in a position to firmly establish the superiority of AFO application in NIBs compared to the LIBs. Regardless, we demonstrated the efficiency of AFO as an anode material for both NIBs and LIBs compared to some mixed oxalate-containing materials used for NIBs and LIBs [11], such as polyanionic $Na_2Fe(C_2O_4)(HPO_4)$ with an OCV of 3.2 V (vs. $Li^+ | Li$) and 3.1 V (vs. $Na^+ | Na$) [48], and its competitive performance with respect to some other materials in NIBs; for example, $CoC_2O_4 \cdot 2H_2O$/rGO with two anodic peaks at 0.25 and 1.25 V [49].

4. Conclusions

We present a first principles study to understand the conversion mechanism in LIBs and NIBs with a FeC_2O_4 anode. This conversion reaction occurs with the formation of a metallic iron phase embedded in a Li/Na oxalate matrix. We invoke both periodic and

non-periodic model calculations. The results obtained using periodic and non-periodic models are similar and indicate a clear trend toward insulator–metal transitions driven by Li/Na addition, with Li addition providing a stronger metallic trend. The conversion process for both Li and Na provides a lower reaction potential than that of NIBs with mixed oxalate anodes. Our study indicates that the capacity of conversion-based materials is much higher than that of the insertion-based anodes involving carbon phases [50].

References

1. Hoke, A.; Brissette, A.; Smith, K.; Pratt, A.; Maksimovic, D. Accounting for lithium-ion battery degradation in electric vehicle charging optimization. *IEEE J. Emerg. Sel. Top. Power Electron.* **2014**, *2*, 691–700. [CrossRef]
2. Whittingham, M.S. Ultimate limits to intercalation reactions for lithium batteries. *Chem. Rev.* **2014**, *114*, 11414–11443. [CrossRef]
3. Jaguemont, J.; Boulon, L.; Dubé, Y. A comprehensive review of lithium-ion batteries used in hybrid and electric vehicles at cold temperatures. *Appl. Energy* **2016**, *164*, 99–114. [CrossRef]
4. Panchal, S.; Dincer, I.; Agelin-Chaab, M.; Fraser, R.; Fowler, M. Design and simulation of a lithium-ion battery at large C-rates and varying boundary conditions through heat flux distributions. *Measurement* **2018**, *116*, 382–390. [CrossRef]
5. Lipu, M.H.; Hussain, A.; Saad, M.; Ayob, A.; Hannan, M. Improved recurrent NARX neural network model for state of charge estimation of lithium-ion battery using pso algorithm. In Proceedings of the 2018 IEEE Symposium on Computer Applications and Industrial Electronics (ISCAIE), Penang, Malaysia, 28–29 April 2018; pp. 354–359.
6. Hwang, J.Y.; Myung, S.T.; Sun, Y.K. Sodium-ion batteries: Present and future. *Chem. Soc. Rev.* **2017**, *46*, 3529–3614. [CrossRef]
7. Kim, D.; Kang, S.H.; Slater, M.; Rood, S.; Vaughey, J.T.; Karan, N.; Balasubramanian, M.; Johnson, C.S. Enabling sodium batteries using lithium-substituted sodium layered transition metal oxide cathodes. *Adv. Energy Mater.* **2011**, *1*, 333–336. [CrossRef]
8. Liu, Y.; He, D.; Han, R.; Wei, G.; Qiao, Y. Nanostructured potassium and sodium ion incorporated Prussian blue frameworks as cathode materials for sodium-ion batteries. *Chem. Commun.* **2017**, *53*, 5569–5572. [CrossRef]
9. Jafta, C.J. Grid scale energy storage: The alkali-ion battery systems of choice. *Curr. Opin. Electrochem.* **2022**, *36*, 101130. [CrossRef]
10. Geng, G.; Keyu, Z.; Qianwen, W.; Libo, Z.; Dingfang, C.; Yaochun, Y. Metal oxalate-based anode materials: A new choice for energy storage materials applied in metal ion batteries. *Prog. Chem.* **2022**, *34*, 434.
11. Yeoh, J.S.; Armer, C.F.; Lowe, A. Transition metal oxalates as energy storage materials. A review. *Mater. Today Energy* **2018**, *9*, 198–222. [CrossRef]
12. Jo, C.H.; Yashiro, H.; Yuan, S.; Shi, L.; Myung, S.T. Conversion chemistry of cobalt oxalate for sodium storage. *ACS Appl. Mater. Interfaces* **2018**, *10*, 40523–40530. [CrossRef]
13. Zhang, K.; Li, Y.; Hu, X.; Liang, F.; Wang, L.; Xu, R.; Dai, Y.; Yao, Y. Inhibitive role of crystal water on lithium storage for multilayer $FeC_2O_4 \cdot xH_2O$ anode materials. *Chem. Eng. J.* **2021**, *404*, 126464. [CrossRef]
14. Poizot, P.; Laruelle, S.; Grugeon, S.; Dupont, L.; Tarascon, J. Nano-sized transition-metal oxides as negative-electrode materials for lithium-ion batteries. *Nature* **2000**, *407*, 496–499. [CrossRef] [PubMed]
15. Cabana, J.; Monconduit, L.; Larcher, D.; Palacin, M.R. Beyond intercalation-based Li-ion batteries: The state of the art and challenges of electrode materials reacting through conversion reactions. *Adv. Mater.* **2010**, *22*, E170–E192. [CrossRef] [PubMed]
16. Yu, S.H.; Lee, S.H.; Lee, D.J.; Sung, Y.E.; Hyeon, T. Conversion reaction-based oxide nanomaterials for lithium ion battery anodes. *Small* **2016**, *12*, 2146–2172. [CrossRef] [PubMed]
17. Grugeon, S.; Laruelle, S.; Dupont, L.; Tarascon, J.M. An update on the reactivity of nanoparticles Co-based compounds towards Li. *Solid State Sci.* **2003**, *5*, 895–904. [CrossRef]

18. Vehmaanperä, P.; Gong, B.; Sit, P.H.L.; Salmimies, R.; Barbiellini, B.; Häkkinen, A. Formation of humboldtine during the dissolution of hematite in oxalic acid–Density functional theory (DFT) calculations and experimental verification. *Clays Clay Miner.* **2021**, *69*, 655–662. [CrossRef]

19. Fan, X.; Zhang, L.; Li, M.; Wang, M.; Zhou, X.; Cheng, R.; Zhou, Y.; Shi, J. *α*-Ferrous oxalate dihydrate: A simple coordination polymer featuring photocatalytic and photo-initiated Fenton oxidations. *Sci. China Mater.* **2016**, *59*, 574–580. [CrossRef]

20. Liu, Z.J.; Liu, W.; Wang, Y.; Guo, M.L. Preparation of *β*-ferrous oxalate dihydrate layered nanosheets by mechanochemical method and its visible-light-driven photocatalytic performance. *Mater. Lett.* **2016**, *178*, 83–86. [CrossRef]

21. Yamada, T.; Sadakiyo, M.; Kitagawa, H. High proton conductivity of one-dimensional ferrous oxalate dihydrate. *J. Am. Chem. Soc.* **2009**, *131*, 3144–3145. [CrossRef]

22. Chen, N.; Zhao, Y.; Li, M.; Wang, X.; Peng, X.; Sun, H.; Zhang, L. $FeC_2O_4 \cdot H_2O$ enables sustainable conversion of hydrogen peroxide to hydroxyl radical for promoted mineralization and detoxification of sulfadimidine. *J. Hazard. Mater.* **2022**, *436*, 129049. [CrossRef] [PubMed]

23. Fu, Q.; Mu, Y.; Yang, L.; Mei, Y.; Wu, M.; Zou, J.P.; Dionysiou, D.D.; Luo, S. Hydroxyl radical streaming from molecular oxygen activation by β-$FeC_2O_4 \cdot 2H_2O$ for efficiently degrading Microcystin-LR. *Appl. Catal. B* **2023**, *321*, 121970. [CrossRef]

24. Müller, H.; Bourcet, L.; Hanfland, M. Iron (II) oxalate dihydrate—Humboldtine: Synthesis, spectroscopic and structural properties of a versatile precursor for high pressure research. *Minerals* **2021**, *11*, 113. [CrossRef]

25. Li, M.; Wang, W.; Yang, M.; Lv, F.; Cao, L.; Tang, Y.; Sun, R.; Lu, Z. Large-scale fabrication of porous carbon-decorated iron oxide microcuboids from Fe–MOF as high-performance anode materials for lithium-ion batteries. *RSC Adv.* **2015**, *5*, 7356–7362. [CrossRef]

26. Lin, X.; Gao, J.; Zhong, K.; Huang, Y.; Yao, H.; Lin, Y.; Zheng, Y.; Huang, Z.; Li, J. Fe/Fe_3C modification to effectively achieve high-performance Si-C anode. *J. Mater. Chem. A* **2022**, *10*, 23103–23112. [CrossRef]

27. Aragón, M.J.; León, B.; Perez Vicente, C.; Tirado, J.L. Synthesis and electrochemical reaction with lithium of mesoporous iron oxalate nanoribbons. *Inorg. Chem.* **2008**, *47*, 10366–10371. [CrossRef]

28. Zhang, K.; Li, Y.; Wang, Y.; Zhao, J.; Chen, X.; Dai, Y.; Yao, Y. Enhanced electrochemical properties of iron oxalate with more stable Li^+ ions diffusion channels by controlling polymorphic structure. *Chem. Eng. J.* **2020**, *384*, 123281. [CrossRef]

29. Keshavarz, F.; Kadek, M.; Barbiellini, B.; Bansil, A. Anodic activity of hydrated and anhydrous Iron (II) oxalate in Li-ion batteries. *Condens. Matter* **2022**, *7*, 8. [CrossRef]

30. Butera, V.; Massaro, A.; Muñoz-García, A.B.; Pavone, M.; Detz, H. d-Glucose Adsorption on the TiO_2 anatase (100) surface: A direct comparison between cluster-based and periodic approaches. *Front. Chem.* **2021**, *9*, 716329. [CrossRef]

31. Soto, F.A.; Ma, Y.; Martinez de la Hoz, J.M.; Seminario, J.M.; Balbuena, P.B. Formation and growth mechanisms of solid-electrolyte interphase layers in rechargeable batteries. *Chem. Mater.* **2015**, *27*, 7990–8000. [CrossRef]

32. Fasulo, F.; Muñoz-García, A.B.; Massaro, A.; Crescenzi, O.; Huang, C.; Pavone, M. Vinylene carbonate reactivity at lithium metal surface: First-principles insights into the early steps of SEI formation. *J. Mater. Chem. A* **2023**, *11*, 5660–5669. [CrossRef]

33. Frisch, M.; Trucks, G.; Schlegel, H.; Scuseria, G.; Robb, M.; Cheeseman, J.; Scalmani, G.; Barone, V.; Petersson, G.; Nakatsuji, H.; et al. *Gaussian 16 revision a. 03. 2016*; Gaussian Inc.: Wallingford, CT, USA, 2016; Volume 2.

34. Perdew, J.P.; Burke, K.; Ernzerhof, M. Generalized gradient approximation made simple. *Phys. Rev. Lett.* **1996**, *77*, 3865. [CrossRef] [PubMed]

35. Grimme, S.; Antony, J.; Ehrlich, S.; Krieg, H. A consistent and accurate ab initio parametrization of density functional dispersion correction (DFT-D) for the 94 elements H-Pu. *J. Chem. Phys.* **2010**, *132*, 154104. [CrossRef]

36. Vidal Vidal, Á.; de Vicente Poutás, L.C.; Nieto Faza, O.; Silva López, C. On the use of popular basis sets: Impact of the intramolecular basis set superposition error. *Molecules* **2019**, *24*, 3810. [CrossRef]

37. Giannozzi, P.; Baroni, S.; Bonini, N.; Calandra, M.; Car, R.; Cavazzoni, C.; Ceresoli, D.; Chiarotti, G.L.; Cococcioni, M.; Dabo, I.; et al. QUANTUM ESPRESSO: A modular and open-source software project for quantum simulations of materials. *J. Phys. Condens. Matter* **2009**, *21*, 395502. [CrossRef] [PubMed]

38. Tominaka, S.; Cheetham, A. Intrinsic and extrinsic proton conductivity in metal-organic frameworks. *RSC Adv.* **2014**, *4*, 54382–54387. [CrossRef]

39. Yuan, Y.x. A modified BFGS algorithm for unconstrained optimization. *IMA J. Numer. Anal.* **1991**, *11*, 325–332. [CrossRef]

40. Weber, M.H.; Lynn, K.G.; Barbiellini, B.; Sterne, P.A.; Denison, A.B. Direct observation of energy-gap scaling law in CdSe quantum dots with positrons. *Phys. Rev. B* **2002**, *66*, 041305. [CrossRef]

41. Tang, Q.; Zhou, Z.; Shen, P. Are MXenes promising anode materials for Li ion batteries? Computational studies on electronic properties and Li storage capability of Ti_3C_2 and $Ti_3C_2X_2$ (X= F, OH) monolayer. *J. Am. Chem. Soc.* **2012**, *134*, 16909–16916. [CrossRef]

42. Lv, X.; Li, F.; Gong, J.; Gu, J.; Lin, S.; Chen, Z. Metallic FeSe monolayer as an anode material for Li and non-Li ion batteries: A DFT study. *Phys. Chem. Chem. Phys.* **2020**, *22*, 8902–8912. [CrossRef]

43. Wang, Y.; Xu, G.; Deng, S.; Wu, Q.; Meng, Z.; Huang, X.; Bi, L.; Yang, Z.; Lu, R. Lithium and sodium decorated graphdiyne as a candidate for hydrogen storage: First-principles and grand canonical Monte Carlo study. *Appl. Surf. Sci.* **2020**, *509*, 144855. [CrossRef]

44. Zhou, F.; Cococcioni, M.; Marianetti, C.A.; Morgan, D.; Ceder, G. First-principles prediction of redox potentials in transition-metal compounds with LDA+ U. *Phys. Rev. B* **2004**, *70*, 235121. [CrossRef]

45. Callaway, J.; Zou, X.; Bagayoko, D. Total energy of metallic lithium. *Phys. Rev. B* **1983**, *27*, 631. [CrossRef]

46. Qian, L.; Yu, T.; Wei, Z.; Chang, B.; Huang, G.; Wang, Z.; Liu, Y.; Sun, H.; Bai, L.; Huang, W. Lower-voltage plateau Zn-substituted Co_3O_4 submicron spheres anode for Li-ion half and full batteries. *J. Alloys Compd.* **2022**, *890*, 161888. [CrossRef]

47. Ang, W.A.; Gupta, N.; Prasanth, R.; Madhavi, S. High-performing mesoporous iron oxalate anodes for lithium-ion batteries. *ACS Appl. Mater. Interfaces* **2012**, *4*, 7011–7019. [CrossRef]

48. Pramanik, A.; Bradford, A.J.; Lee, S.L.; Lightfoot, P.; Armstrong, A.R. $Na_2Fe(C_2O_4)(HPO_4)$: A promising new oxalate-phosphate based mixed polyanionic cathode for Li/Na ion batteries. *J. Phys. Mater.* **2021**, *4*, 024004. [CrossRef]

49. Zhang, Y.; Wang, C.; Dong, Y.; Wei, R.; Zhang, J. Understanding the high-performance anode material of $CoC_2O_4 \cdot 2H_2O$ microrods wrapped by reduced graphene oxide for lithium-ion and sodium-ion batteries. *Chem. Eur. J.* **2021**, *27*, 993–1001. [CrossRef]

50. Kim, H.; Kim, D.I.; Yoon, W.S. Challenges and design strategies for conversion-based anode materials for lithium-and sodium-ion batteries. *J. Electrochem. Sci. Technol.* **2022**, *13*, 32–53. [CrossRef]